



# Forward bias operation of silicon photonic Mach Zehnder modulators for RF applications

RUI LIN CHAO,<sup>1,2</sup> JIN WEI SHI,<sup>1,3</sup> ADITYA JAIN,<sup>1,\*</sup> TAKAKO HIROKAWA,<sup>1,4</sup> AKHILESH S.P. KHOPE,<sup>1,4</sup> CLINT SCHOW,<sup>1,4</sup> J.E. BOWERS,<sup>1,4</sup> ROGER HELKEY,<sup>1</sup> AND JAMES F. BUCKWALTER<sup>4</sup>

<sup>1</sup>The Institute for Energy Efficiency, University of California Santa Barbara, California, 93106, USA

<sup>2</sup>Department of Photonics, National Chiao Tung University, Hsinchu 300, Taiwan

<sup>3</sup>Department of Electrical Engineering, National Central University, Jungli, 320, Taiwan

<sup>4</sup>Department of Electrical and Computer Engineering, University of California Santa Barbara, California, 93106, USA

\*ajain17@ucsb.edu

**Abstract:** In this paper, we demonstrate that forward bias (+0.9V) of a high-speed silicon (Si) optical Mach-Zehnder Modulator (MZM) increases the radio-frequency (RF) link gain by 30 dB when compared to reverse bias operation (-8V). RF applications require tunable, narrow-band electro-optic conversion with high gain to mitigate noise of the optical receiver and realize high RF spur-free dynamic range. Compared to reverse bias, the forward bias gain rolls off more rapidly but offers higher RF link gain improvement of more than 13.2 dB at 20 GHz. Furthermore, forward bias is shown to result in comparable spurious-free dynamic range (SFDR: 104.5 dB.Hz<sup>2/3</sup>). We demonstrate through an analytical dc transfer curve the existence of simultaneous high gain and OIP3 and verify the theoretical results with measurement under forward bias at a bias point of around +0.9 V.

© 2017 Optical Society of America

**OCIS codes:** (250.4110) Modulators; (250.5300) Photonic integrated circuits.

## References and links

1. R. A. Soref, and B. R. Bennett and Brian R. Bennett, "Electrooptical effects in silicon," *IEEE J. Quantum Electron.* **23**(1), 123–129 (1987).
2. S. J. Spector, M. W. Geis, G.R. Zhou, M. E. Grein, F. Gan, M.A. Popovic, J. U. Yoon, D. M. Lennon, E. P. Ippen, F. X. Kartner and T. M. Lyszczarz, "CMOS compatible dual output silicon modulator for analog signal processing," *Opt. Express* **16**(15), 11027–11031 (2008).
3. Q. Xu, S. Manipatruni, B. Schmidt, J. Shakya, and M. Lipson, "12.5 Gbit/s carrier-injection-based silicon microring silicon modulators," *Opt. Express* **15**(2), 430–436 (2007).
4. W. M. J. Green, M. J. Rooks, L. Sekaric, and Y. A. Vlasov, "Ultra-compact, low RF power, 10 Gb/s silicon Mach-Zehnder modulator," *Opt. Express* **15**(25), 17106–17113 (2007).
5. G. R. Zhou, M. W. Geis, S. J. Spector, F. Gan, M. E. Grein, R. T. Schulein, J. S. Orcutt, J. U. Yoon, D. M. Lennon, T. M. Lyszczarz, E. P. Ippen, and F. X. Kartner, "Effect of carrier lifetime on forward-biased silicon Mach-Zehnder modulators," *Opt. Express* **16**(8), 5218–5226 (2008).
6. S. J. Spector, C. M. Sorace, M. W. Geis, M. E. Grein, J. U. Yoon, T. M. Lyszczarz, E. P. Ippen, and F. X. Kartner, "Operation and Optimization of Silicon-Diode-Based Optical Modulators," *IEEE J. Quantum Electron.* **16**(1), 165–172 (2010).
7. S. Akiyama, M. Imai, T. Baba, T. Akagawa, N. Hirayama, Y. Noguchi, M. Seki, K. Koshino, M. Toyama, T. Horikawa, and T. Usuki, "Compact PIN-Diode-Based Silicon Modulator Using Side-Wall-Grating Waveguide," *IEEE J. Quantum Electron.* **19**(6), 74–84 (2013).
8. A. Ayazi, T. B. Jones, Y. Liu, A. E. J. Lim, and M. Hochberg, "Linearity of silicon ring modulators for analog optical links," *Opt. Express* **20**(12), 13115–13122 (2012).
9. L. Chen, J. Chen, J. Nagy, and R. M. Reano, "Highly linear ring modulator from hybrid silicon and lithium niobate," *Opt. Express* **23**(10), 13255–13264 (2015).
10. C. Zhang, P. A. Morton, J. B. Khurgin, J. D. Peters, and J. E. Bowers, "Ultralinear heterogeneously integrated ring assisted Mach Zehnder interferometer modulator on silicon," *Optica* **3**(12), 1483–1488 (2016).
11. C. Zhang, P. A. Morton, J. B. Khurgin, J. D. Peters, and J. E. Bowers, "Highly linear heterogeneous-integrated Mach-Zehnder interferometer modulators on Si," *Opt. Express* **24**(17), 19040–19047 (2016).
12. X. Xiao, H. Xu, X. Li, Z. Li, T. Chu, Y. Yu, and J. Yu, "High-speed, low loss silicon Mach Zehnder modulators with doping optimization," *Opt. Express* **21**(4), 4116–4125 (2013).

13. A. Khilo, C. M. Sorace, and F. X. Kartner, "Broadband linearized silicon modulator," *Opt. Express* **19**(5), 4485–4500 (2011).
14. M. Streshinsky, A. Ayazi, Z. Xuan, A. E. J. Lim, G. Q. Lo, T. B. Jones, and M. Hochberg, "Highly linear silicon traveling wave Mach-Zehnder carrier depletion modulator based on differential drive," *Opt. Express* **21**(3), 3818–3825 (2013).
15. K. Solehmainen, M. Kapulainen, M. Harjanne, and T. Aalto, "Adiabatic and Multimode Interference Couplers on Silicon-on-Insulator," *IEEE Photon. Technol. Lett.* **18**(21), 2287–2289 (2006).

## 1. Introduction

Development of silicon-based RF and microwave photonics has the potential to realize low-cost optical devices integrated in a CMOS-compatible process. However, to date, silicon-based microwave photonic modulators have demonstrated considerably lower SFDR than Lithium Niobate devices. Research efforts have investigated linearization of silicon-based modulators through the free carrier plasma dispersion effect by different concentration of doping profile to control refraction index within the waveguide [1]. Most published work focuses on carrier depletion under reverse bias conditions for wide 3-dB electrical-to-optical (E-O) bandwidth (>20 GHz) and high-speed data transmission (>50 Gb/s) because of the reduced junction capacitance [2–11]. But reverse bias operation has the tradeoff of relatively weak variation in carrier density (refractive index) per unit length, which results in high drive voltage ( $V_\pi > 5V$ ) and long active device length ( $L > 1$  mm) in silicon. For silicon photonic MZMs, the typical product of drive voltage and device active length ( $V_\pi L$ ) is usually around 2 V.cm [12] and results in microwave photonic devices that either suffer from high electrode attenuation that reduce the frequency cut-off or short devices that exhibit low gain, and thereby, high noise figure.

Alternatively, forward bias of the waveguide in an MZM provides significantly higher gain, lower  $V_\pi$  and comparatively short device length with an extremely small  $V_\pi L$  product (0.024 V.cm) [5]. Higher RF link gain enables low noise figure and thereby improves the Signal to Noise Ratio without the need for additional amplification before the modulator. An input amplifier adds complexity and cost to the system and increases the overall noise figure and power requirements. The 3-dB E-O bandwidth is degraded under these conditions due to the slow diffusion current in p-n junction [6]. Prior work investigated pre-emphasis to compensate the roll-off in the frequency response of the MZM under forward bias for high-speed (50 Gb/s) operation [7]. In narrowband RF applications, the 3-dB bandwidth is not a critical design requirement since the system might be tuned reactively to a particular band.

In this work, we demonstrate that forward bias of a silicon photonic (SiP) Mach-Zehnder modulator (MZM) at around +0.9 V exhibits up to 40 dB more RF link gain without sacrificing spurious-free dynamic range (SFDR). The SFDR is around (104.5 dB.Hz<sup>2/3</sup>) and comparable to results found under reverse bias conditions (-8V). The modulation of output power versus bias voltage becomes more efficient at nearly forward bias [5], which is observed in the MZM DC transfer curve. By analyzing the transfer curves, we observe that the optimum bias points correspond to a maximum of first derivative and minimum in third derivative in the measured DC transfer curve, are very close and exist at around +0.9 V. At this bias point, the maximum RF link gain is -14.7 dB at 1 GHz and the corresponding SFDR performance is 104.5 dB.Hz<sup>2/3</sup>.

## 2. Theory of optimized bias points in MZM

The transfer function of the MZM is described in terms of a voltage-dependent complex effective index,  $n_{eff}^{real}(V) - in_{eff}^{imag}(V)$ , for the individual arm. The two arms of the MZM are considered identical and described by a nonlinear voltage-dependent phase change  $\phi(V) = n_{eff}^{real}(V) \frac{2\pi}{\lambda}$  and attenuation  $\alpha(V) = n_{eff}^{imag}(V) \frac{4\pi}{\lambda}$ . To verify our results with experiment, we assume that the bias voltage of one arm is fixed at a voltage  $V_{DC}$ . The output power of an MZM of length  $L$  in output 1 and output 2 can be written as the sum and difference of the propagating

waves in both the arms

$$P_{1,2} = P_{in} \left| \frac{e^{-i(n_{eff}^{real}(V) - in_{eff}^{imag}(V))\frac{2\pi L}{\lambda}} e^{-i\phi_H} \pm e^{-i(n_{eff}^{real}(V_{DC}) - in_{eff}^{imag}(V_{DC}))\frac{2\pi L}{\lambda}}}{2} \right|^2 \quad (1)$$

$P_{in}$  is the input power of the MZM after subtracting the insertion loss resulting from the edge coupling and the waveguide bend loss. The complex refractive index is bias dependent for the doped rib waveguide. We assume that one arm is fixed at a reverse bias voltage. Substituting  $\phi(V) = n_{eff}^{real}(V)\frac{2\pi}{\lambda}$  and attenuation  $\alpha(V) = n_{eff}^{imag}(V)\frac{4\pi}{\lambda}$ , we obtain a simplified expression as [13]

$$\frac{P_1}{P_{in}} = \underbrace{\left[ \left( \frac{e^{-\frac{\alpha(V)L}{2}} - e^{-\frac{\alpha(V_{DC})L}{2}}}{2} \right)^2 + e^{-\left( \frac{\alpha(V)L + \alpha(V_{DC})L}{2} \right)} \right]}_{T_1(V)} \left( \cos \left( \frac{\phi(V)L - \phi(V_{DC})L + \phi_H}{2} \right) \right)^2 \quad (2)$$

$$\frac{P_2}{P_{in}} = \underbrace{\left[ \left( \frac{e^{-\frac{\alpha(V)L}{2}} - e^{-\frac{\alpha(V_{DC})L}{2}}}{2} \right)^2 + e^{-\left( \frac{\alpha(V)L + \alpha(V_{DC})L}{2} \right)} \right]}_{T_2(V)} \left( \sin \left( \frac{\phi(V)L - \phi(V_{DC})L + \phi_H}{2} \right) \right)^2 \quad (3)$$

For a silicon PN phase shifter operating on the principle of plasma dispersion effect,  $\phi(V)$  and  $\alpha(V)$  are non-linear functions of applied DC bias and can be written as

$$\phi(V) = \phi_A V + \phi_B V^2 + \phi_C V^3 + \dots \quad (4)$$

$$\alpha(V) = \alpha_A + \alpha_B V + \alpha_C V^2 + \alpha_D V^3 + \dots \quad (5)$$

The resulting transfer function is highly nonlinear with several tunable parameters such as  $V_{DC}$ , heater phase shift  $\phi_H$ , and  $L$ . It has been noted in previous work [13] that the second and third-order non-linearity can be cancelled with an appropriate combination of the above three parameters. In general, second harmonic distortion (SHD) depends on the non-linearity of the attenuation function ( $\alpha_A, \alpha_B, \alpha_C \dots$ ) while the intermodulation distortion (IMD) depends on the non-linearity of the phase function ( $\phi_A, \phi_B, \phi_C \dots$ ). Here, we only monitor the optical output 1 and consider that similar results could be reached for output 2. The transfer function for output 1 ( $T_1(V) = \frac{P_1(V)}{P_{in}}$ ) is expanded as a Taylor series at  $V_{DC}$  as [14]

$$T_1(V) = T_1 \Big|_{V=V_{DC}} + (V - V_{DC}) \frac{dT_1}{dV} \Big|_{V=V_{DC}} + \frac{(V - V_{DC})^2}{2!} \frac{d^2 T_1}{dV^2} \Big|_{V=V_{DC}} + \dots \quad (6)$$

If we apply two RF tones at  $f_1$  and  $f_2$  to one of the arms, ( $V = V_{DC} + v_0 \sin(2\pi f_1 t) + v_0 \sin(2\pi f_2 t)$ ), we obtain the magnitude of fundamental ( $T_1^{(f_1)}(V)$ ) and third-order intermodulation distortion (IMD) term ( $T_1^{(2f_2 - f_1)}(V)$ ) as

$$T_1^{(f_1)}(V) = v_0 \frac{dT_1}{dV} \Big|_{V=V_{DC}} + \frac{3}{8} v_0^3 \frac{d^3 T_1}{dV^3} \Big|_{V=V_{DC}} + \dots \quad (7)$$

$$T_1^{(2f_2 - f_1)}(V) = \frac{1}{8} v_0^3 \frac{d^3 T_1}{dV^3} \Big|_{V=V_{DC}} + \dots \quad (8)$$

The detected RF output power is

$$P_{out}^{RF}(V) = (T_1(V)P_{in}R_{PD})^2 R_{mod}R_D \quad (9)$$

$R_{PD}$  is the responsivity of the detector in A/W,  $R_{mod}$  is the modulator load resistance and  $R_D$  is the Photo diode resistance. Finally, the detected small signal RF power at each harmonic can be written as:

$$P_{(f_1)out}^{(RF)}(V) = (P_{in}v_0 \frac{dT_1}{dV} \Big|_{V=V_{DC}} + P_{in} \frac{3}{8} v_0^3 \frac{d^3T_1}{dV^3} \Big|_{V=V_{DC}} + \dots)^2 (R_{PD})^2 R_{mod}R_D \quad (10)$$

$$P_{(f_1)out}^{(RF)}(V) \approx (P_{in}v_0 \frac{dT_1}{dV} \Big|_{V=V_{DC}})^2 (R_{PD})^2 R_{mod}R_D \quad (11)$$

Similarly, the detected small signal RF power at the IMD frequency is

$$P_{(2f_1-f_2)out}^{(RF)}(V) \approx (P_{in} \frac{1}{8} v_0^3 \frac{d^3T_1}{dV^3} \Big|_{V=V_{DC}})^2 (R_{PD})^2 R_{mod}R_D \quad (12)$$

For an analog link, we require that the slope of the transfer function must be maximized (Eq. (11)), while the IMD products must be minimized (Eq. (12)). The RF link is characterized by third-order intercept point (IP3), the intersection of the extrapolated small signal response of the fundamental and the third-order distortion [13]. The input IP3 (IIP3) is

$$IIP3(dBm) = 10 \log_{10} \left( \frac{\frac{dP_1}{dV} \Big|_{V=V_{DC}}}{\frac{d^3P_1}{dV^3} \Big|_{V=V_{DC}}} \frac{8}{R_{in}} \right) + 30 \quad (13)$$

Here  $R_{in}$  is the input resistance. IIP3 is maximized when the IMD is zero. In the following section, we will analyze the measured DC transfer curve based on the above-mentioned equations to optimize the linearity and RF link gain of the MZM.

### 3. Device structure and analysis of DC measurement results

Figure 1 shows the conceptual diagram of the modulator under test. The active length of the device is 1 mm long and comprises two p-n junction phase shifter arms at the input (I) for modulating the optical signal and one adiabatic 3-dB directional coupler at the output (O). The modulated optical power is split into two complementary output ports [2, 15]. In our modulator layout, we have incorporated the U-bends in the output waveguides and intentionally route the I/O ports on the same side of chip. During optical alignment, an array of cleaved fiber tips for simultaneous I/O light injection and collection, respectively, are mounted on Silicon-based V-grooves array (DTS-0083, OZ optics) with equal spacing ( $127 \mu m$ ), which is matched with the interval between I/O ports on modulator. This design eliminates fiber-to-fiber alignment on different sides of the chip to simplify the alignment process. Each phase shifter is controlled by a pair of GS (ground, signal) electrodes for feeding the RF signal into the arm. The G pad of each optical phase shifter is shorted together. A resistor-based heater is installed nearby one of the optical output arms. With an independent DC voltage, we can then add the additional phase shift for the optical path to manipulate the DC transfer curves. Figure 2 shows the microphotograph of the device under test. The MZM under test has 1 mm active device length and the GSGSG

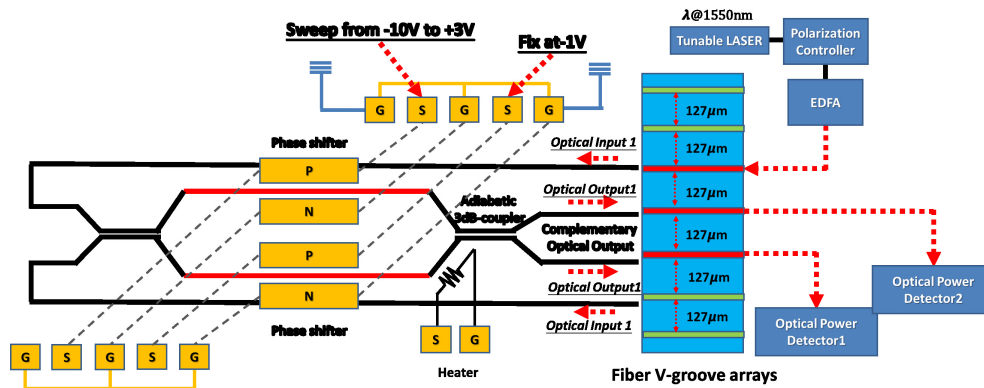


Fig. 1. Conceptual picture of modulator under test and measurement setup for DC transfer curve. EDFA: Erbium-doped Optical Fiber Amplifier.

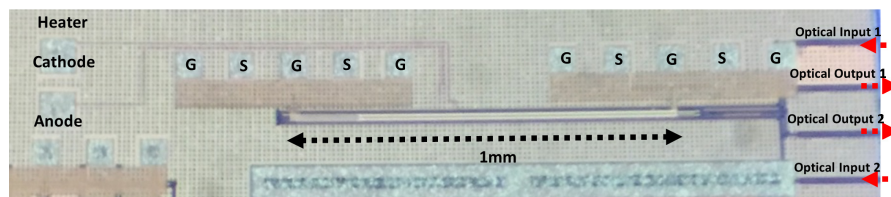


Fig. 2. Picture of the tested device from AIM Photonics, Rochester, NY, USA. Process Design Kit (PDK) 0.5a. Two optical inputs/outputs are on the same side of chip.

pads on each side of the MZM is compatible with a fully-differential RF signal feed and  $50\Omega$  termination through the use of GSGSG dual RF probes, respectively.

The dc bias point of the MZM is the most important characteristics to optimize RF performance and can be analyzed from the dc transfer curve [13, 14]. As shown in Fig. 1, we measured the single-ended dc transfer curve by fixing one arm at  $-1\text{V}$ , and then sweeping the other arm from  $-10\text{V}$  to  $+3\text{V}$  (from reverse bias to forward bias) to record the output optical power. The launched optical power is fixed  $+22\text{ dBm}$  at  $1550\text{ nm}$  wavelength. We have also applied different heater bias voltages ( $0$  to  $10\text{ V}$ ) to investigate the influence of additional phase change on the DC transfer curve. Figure 3(a) shows four typical measured transfer curves for four different heater voltages ( $0$ ,  $4$ ,  $8$ , and  $10\text{ V}$ ). Due to the short length and high  $V_\pi$  ( $\sim 25\text{ V}$ ) of our modulator in reverse bias regime, induced phase shift by the heater ( $0$ - $8\text{V}$ ) is not visible in the transfer curve and a relatively flat response is obtained in the output optical power. In addition, according to the maximum value of output power in transfer curve ( $+5\text{ dBm}$ ), the fiber-to-fiber optical insertion loss of whole MZM chip is around  $17\text{ dB}$ .

Alternatively, the device demonstrates dramatic change in the output optical power in the transfer curves as a function of bias voltage in the forward bias regime ( $0\text{V}$  to  $+3\text{V}$ ). Figure 3(b) highlights the zoom in transfer curve from Fig. 3(a) under forward bias. The change in the transfer curve is attributed to the forward bias current, which induces significant change in the carrier density (refractive index) inside optical waveguide as compared to MZM under reverse bias operation. The asymmetry between two optical waveguides inside the MZM due to process variation might be compensated by extra phase shift from the heater. According to these static measurement results, we can conclude that operating in forward bias provides larger modulation efficiency and a higher radio-frequency (RF) link gain.

Based on Eq. (11) and Eq. (12), these transfer curves determine the optimized forward bias

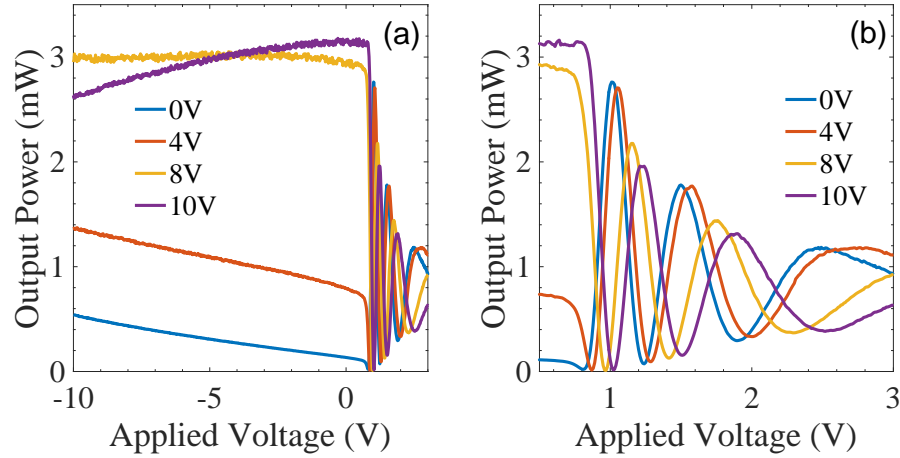


Fig. 3. (a) Bias dependent (-10 to +3 V) DC transfer curves of MZM under four different heater voltage (0, 4, 8 and 10V). Results are shown for Optical output 1. (b) The zoom-in picture of transfer curves at forward bias regime.

operation point for simultaneous performances of high linearity and large RF link gain. From the measured transfer curves, the bias voltages are calculated for the maximum gain based on Eq. (11). The output power  $P_1(V)$  of the MZM under different heater voltages (0, 4, 8, and 10 V) shown in Fig. 3(a)(b) is replotted again in Fig. 4(a-d). The slope of the smoothed transfer function (i.e. gain) is given in Fig. 4(e-h). For reference, we have also plotted the smoothed third derivative of the transfer curve Fig. 4(i-l) representing the IMD products based on Eq. (12).

Table 1.  $V_{gain,max}$  and  $V_{IMD=0}$  under Different Heater Voltages

$V_{heater}(V)$	$V_{gain,max}(V)$	$V_{IMD=0}(V)$
0	0.93	0.88
4	0.97	0.91
8	0.88	0.84
10	0.93	0.88

Ideally, we select a point on the transfer curve where the magnitude of the first derivative is maximized (red circles in Fig. 4(a-l)) while the third derivative (blue circles in Fig. 4(a-l)) is simultaneously minimized. Surprisingly, these two conditions happen at similar forward bias voltages and at consistent voltages as a function of heater voltage. For example, maximum gain occurs for a zero-heater voltage at a forward bias of  $V_{gain,max}=0.93$  V (red circle in Fig. 4(e)), while the IMD products are minimized at  $V_{IMD=0}=0.88$  V (blue circle in Fig. 4(i)). For reference, we have listed all the values of  $V_{gain,max}$  (red circles in Fig. 4(e-h)) and  $V_{IMD=0}$  (blue circles in Fig. 4(i-l)) in Table 1 for different heater voltages.

#### 4. Dynamic measurement results

The E-O frequency response of the MZM is measured with a lightwave component analyzer (LCA; Agilent N4373C). Figure 5(a) shows the conceptual diagram of our experimental setup. Under dynamic measurement, the MZM is under single-ended operation and fed by a GSG probe while the other port is terminated in a 50  $\Omega$  load. Figure 6 shows the measured bias

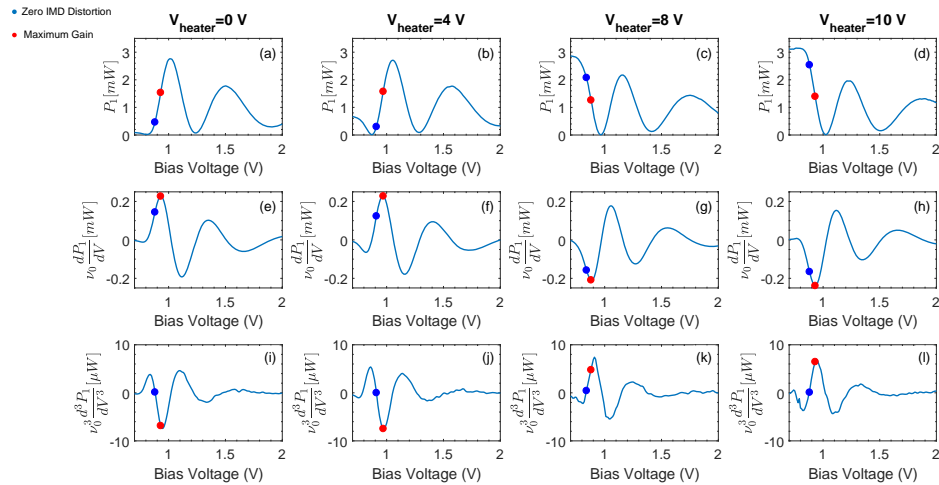


Fig. 4. (a-d) Output power (mW) as a function of the forward bias, applied to one of the MZM arms under four different heater voltage (0, 4, 8, and 10V). (e-h) First derivative of the forward biased MZM transfer curve (mW) under four different heater voltage (0, 4, 8, and 10V). (i-l) Third derivative of the forward biased MZM transfer curve ( $\mu\text{W}$ ) under four different heater voltage (0, 4, 8, and 10V). Second arm is reverse biased at -1V for all cases and the small signal voltage amplitude is taken to be 0.01 V. Red Circles shows the position of maximum gain while the blue circles show the bias voltage where the Intermodulation Distortion is zero.

dependent E-O frequency responses under 0 V heater voltage. The measured E-O frequency responses at high reverse bias regime (-8V), which shows a 3-dB E-O bandwidth of 19.85 GHz, is also given for comparison. The forward bias operation has a significantly smaller -3 dB bandwidth while the measured E-O frequency response shows a much higher reference level of output power ( $> 13.1$  dB at around +0.9V) over the whole span of measurement frequency (DC to 20 GHz) than under -8 V bias. Furthermore, around 48.7 dB enhancement in reference level power is observed at low frequency. However, the reference level is not always indicative of the actual gain present at a certain RF frequency due to the difference in optical power reaching the Photodetector for different bias voltages. To remedy this problem, and investigate the Gain and IMD generation, we have measured the two-tone response as a function of input power.

Figure 5(b) shows the schematic illustration of experimental setup. We performed two-tone measurements with the RF signal input at 1 GHz and 1.1 GHz. To further reduce the noise floor during experiment, a high power (+18 dBm) distributed feedback (DFB) laser (APIC LM-1550-168-80) with a low relative intensity noise (RIN) performance replaces the optical light source used in the LCA and dc transfer curve measurements.

The input RF power is swept from -10 to +20 dBm and the launched optical power from the optical input port of MZM is fixed at +18 dBm. A photoreceiver module (Agilent 11982 A) inside which RF power will be amplified around 18 dB, is placed at the output of the MZM to convert the modulated optical envelope into RF signal. The photo-generated RF tones at fundamental (1 and 1.1 GHz) and third-order (0.9 and 1.2 GHz) frequencies are recorded by the electrical spectrum analyzer (Agilent E4407B). Figure 7(a,b) show the two-tone measurement results of our MZM operated under optimized forward bias at around +0.9 V for highest linearity and -8 V reverse bias, respectively. The heater bias is fixed at 0 V. The bias points chosen for the measurement (0.9V) correspond to the optimum bias for  $V_{gain,max}$ ,  $V_{IMD=0}$  as discussed in Table 1. Compared with reverse bias (-8V), forward bias operation exhibits not only

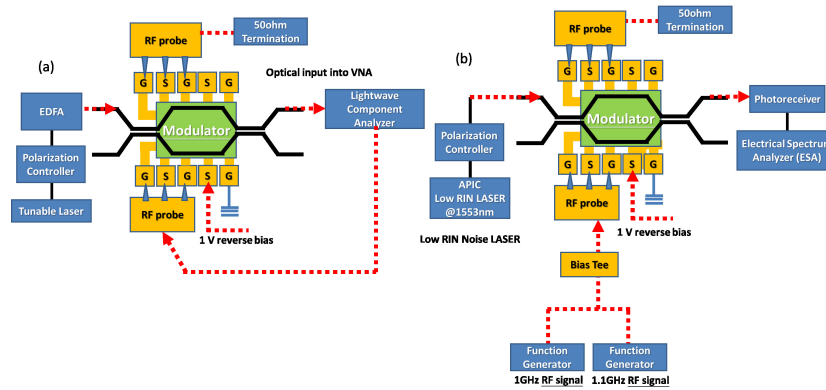


Fig. 5. (a) Experimental setup for E-O responses measurement. (b) Experimental setup for two-tone measurement. EDFA: Erbium-doped Optical Fiber Amplifier

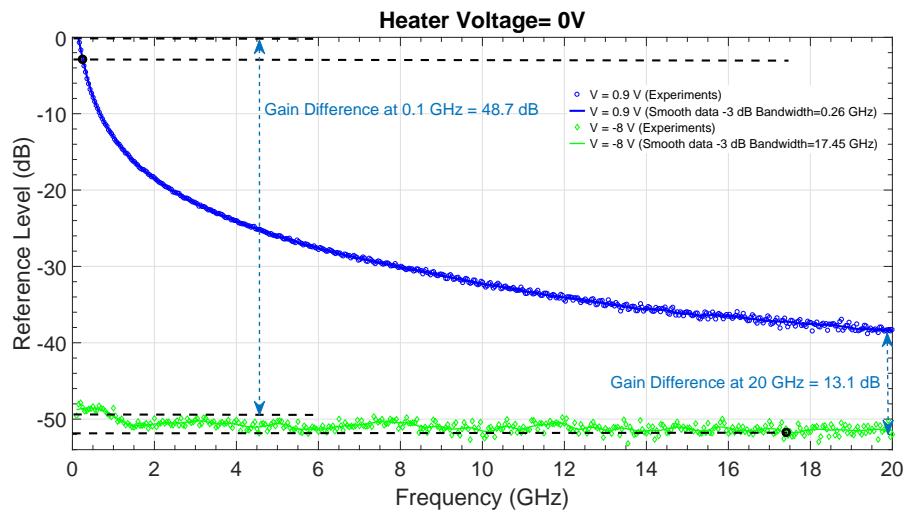


Fig. 6. Measured bias dependent E-O frequency responses for forward biased +0.9V and -8V reverse biased MZM at 0V heater voltage. -3dB bandwidth for each curve is marked by a hollow black circle in the figure and the numeric value is listed in the legend.

a 28.3 dB enhancement in RF gain but also similar SFDR at around 88 dB. By normalizing our measured noise floor (-122 dBm) with the resolution bandwidth (300 Hz) in electrical spectrum analyzer (ESA), the SFDR becomes  $104.5 \text{ dB.Hz}^{2/3}$ . For reference, we have also plotted the SFDR measurement at 10 GHz in Fig. 7(c). Although the gain is reduced at 10 GHz, we still observe a SFDR performance around 69 dB ( $85 \text{ dB.Hz}^{2/3}$  normalized to the noise floor) and a gain value of -45.6 dB in Fig. 7(c). While we do see a 19 dB decrease in our dynamic range, the measured gain of -45.6 dB is still comparable to the gain value of -41.8 dB, observed for reverse bias condition at 1 GHz.

As shown in Table 1, our theoretical analysis of transfer curves suggests that the highest linearity (SFDR) and RF gain occurs at +0.9 V bias (zero heater bias) and the other forward bias point would suffer from more significant distortion and decreased gain. Figure 8 plots the two-tone measurement results at 0.6 V forward bias for comparison. As can be seen, the SFDR value degrades significantly (from 88 to 77 dB).

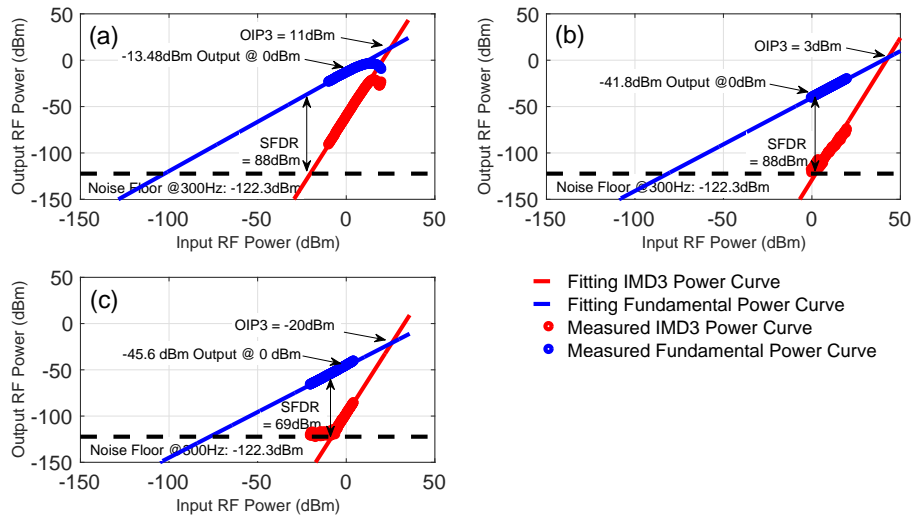


Fig. 7. Two-tone measurement results of MZM at (a) +0.9 V at 1 GHz and (b) -8 V at 1 GHz. (c) +0.8 V at 10 GHz. The heater voltage is fixed at 0V. IMD3: Third-order intermodulation distortion. OIP3: Third-order intercept point. SFDR: Spurious-free dynamic range

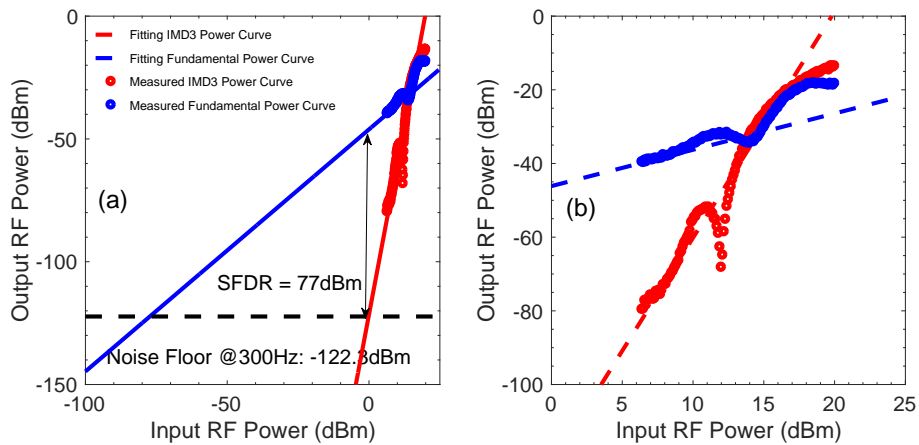


Fig. 8. (a) Two-tone measurement results of MZM at +0.6 V. The heater voltage is fixed at 0V. (b) The zoom-in picture when the input RF power is near OIP3. IMD3: Third-order intermodulation distortion. OIP3: Third-order intercept point. SFDR: Spurious-free dynamic range

## 5. Conclusion

RF operation of a SiP MZM under forward bias point (around + 0.8V) demonstrated significant improvement in RF gain ( 28.3 dB at 1 GHz) and exhibits high linearity (SFDR: 104.5 dB.Hz<sup>2/3</sup>) at 1 GHz compared with reverse bias operation (-8V). Analyzing the dc transfer curve of the MZM demonstrated both the higher gain and IIP3. This result suggests RF applications of SiP MZMs where tuning between forward and reverse bias might be possible for high SFDR with large gain variation.

**Funding**

Air Force Research Laboratory FA8650-15-2-5220.

**Acknowledgments**

We would like to thank AIM Photonics for providing their foundry services and Analog Photonics company for providing their photonic components as part of the AIM PDK. We would like to thank Doug Coolbaugh and Hmayak Bagramian at SUNY Polytechnic Institute, and Ben Moss and Erman Timurdogan at Analog Photonics.